NASA
Technical
Paper
1931

September 1982

Comparison of Two- and Three-Dimensional Flow Computations With Laser Anemometer Measurements in a Transonic Compressor Rotor

Rodrick V. Chima and
Anthony J. Strazisar

Property of U. S. Air Force
AEDC LIBRARY
F40600-81-C-0004

NASA
Technical
Paper
1931

1982

Comparison of Two- and Three-Dimensional Flow Computations With Laser Anemometer Measurements in a Transonic Compressor Rotor

Rodrick V. Chima and
Anthony J. Strazisar

Lewis Research Center
Cleveland, Ohio

NASA
National Aeronautics
and Space Administration

Scientific and Technical
Information Branch

Summary

Two- and three-dimensional inviscid solutions for the flow within a transonic axial compressor rotor at design speed are compared with probe and laser anemometer measurements at the near-stall and maximum-flow operating points. Experimental details of the laser anemometer measurement system are described. Computational details of the two-dimensional axisymmetric stream function solution and the three-dimensional full Euler solution are also described. Upstream of the rotor the two- and three-dimensional solutions for radial distribution of relative Mach number and total pressure agree well with the data. Within the bow wave system and the blade row the axisymmetric two-dimensional solution shows only qualitative agreement with the data. Comparisons are made between relative Mach number and flow angle contours, shock location, and shock strength as measured and as predicted by the three-dimensional code. Comparisons near the tip for the near-stall case show excellent agreement. Comparisons at maximum flow show reasonably good agreement at all spanwise locations but also some disagreement due to viscous effects. Downstream of the rotor the inviscid computations agree with each other but predict higher pressure ratios than those measured. Euler codes typically require a downstream pressure as input. Since that pressure controls the computed mass flow and shock system, it must be consistent with an inviscid solution. A procedure for using an efficient axisymmetric code to generate downstream pressure input for more costly Euler codes is discussed. A film supplement shows convergence of the Euler code for the maximum-flow case and calculation of the near-stall case as the time-accurate response of the maximum-flow solution to changes in boundary conditions.

Introduction

Computational and experimental techniques for the study of flows in turbomachinery are evolving concurrently and are mutually supportive. Experiments provide data for empirical correlations of phenomena that cannot yet be computed, such as turbulence. Experimental data may also be used to verify direct computations of flow phenomena. Computational methods can determine thermodynamic quantities that cannot be measured by optical techniques. Computational methods are also becoming important tools for the development of advanced turbomachine components and can be used to screen new designs before resorting to more costly experiments.

Advances in both computational and experimental fluid mechanics have been paced largely by advances in electronics, particularly in digital data acquisition and processing. In a 1958 NACA report (ref. 1), tip static pressures were measured in a transonic compressor rotor by using oscilloscope traces of signals from four pressure transducers embedded in the shroud. Experimentalists now rely on digital data acquisition and reduction systems coupled with traversing pressure and temperature probes for pitchwise-averaged flow measurements upstream and downstream of rotors (ref. 2). Two-dimensional throughflow analysis codes like reference 3 are the computational counterparts of these probe measurements. Current data-processing equipment coupled with electro-optical sensors allows the experimentalist to make detailed maps of the core flow in rotating compressors (refs. 4 and 5). Three-dimensional analysis codes like reference 6 are the computational counterparts of current laser anemometer measurements. Experimentalists are just beginning to take measurements inside the viscous layers on blade rows. Similarly, computational methods are now being developed to analyze two-dimensional viscous flows in cascades (ref. 7). It seems likely that the latest generation of supercomputers and continuing advances in instrumentation will allow both computational and experimental work to progress even further and that the resulting gains in understanding will lead to improvements in turbomachinery performance.

It is important to note that the early experimental and analytical work is still extremely important. In fact this report relies heavily on all of references 1 to 6 mentioned above. Before going into the details of the present work, it may be of interest to review current literature comparing optical measurements and computations of flows in turbomachinery.

Optical techniques that have been used for flow measurements in turbomachinery include holographic interferometry (ref. 8), the gas fluorescence technique (ref. 9), the laser two-focus technique (L2F, also called laser transit anemometry or LTA) (refs. 10 and 11), and laser anemometry (LA, also called laser Doppler velocimetry or LDV) (refs. 4 and 5). The LA technique reported in reference 5 was used in the present work.

Computational methods used to calculate flows in turbomachinery include two-dimensional throughflow codes (refs. 3, 12, and 13); two-dimensional, steady blade-to-blade codes (refs. 14 and 15); two-dimensional, unsteady blade-to-blade codes (refs. 13 and 16); quasi-three-dimensional codes (refs. 13 and 14); and fully three-dimensional codes (refs. 6 and 17). The two-dimensional throughflow code in reference 3 and the three-dimensional code in reference 6 were used in the present work.

The following references compare optical measurements with computations of flows in turbomachinery. Several references have compared computations to L2F measurements in a transonic rotor designed and tested at DFVLR. Reference 12 compares these measurements with throughflow calculations at a full-speed operating point. Reference 14 compares them with a quasi-three-dimensional solution at a subsonic part-speed operating point, and reference 13 compares them with a quasi-three-dimensional time-marching solution at three transonic operating conditions. A fully three-dimensional solution for transonic flow in the DFVLR rotor is presented in reference 17. Comparisons between LTA measurements and steady blade-to-blade solutions of the flow in a low-speed, four-stage General Electric research rotor are given in reference 15. Reference 16 gives an early comparison between LA measurements and a steady blade-to-blade solution in a GE transonic fan. Reference 18 compares gas fluorescence measurements with a three-dimensional time-marching solution for a NASA low-aspect-ratio transonic fan.

The present work compares conventional probe measurements, LA measurements, two-dimensional through-flow computations, and three-dimensional Euler computations of transonic flows in a NASA-designed core compressor inlet rotor. These comparisons are made at design speed at two operating points, a near-stall point and a maximum-flow point. Comparisons between measured and computed data are made for total pressures, relative Mach numbers, and relative flow angles along grid lines, for nominal relative Mach numbers on the blade surfaces, for contour plots of relative Mach numbers and flow angles on grid planes, for shock locations and strengths, and for mass flows and total pressure ratios. These comparisons are intended to demonstrate the capabilities of the analysis codes for predicting two widely different flow conditions in an actual machine.

In reference 8 similar comparisons were made between LA data and a three-dimensional Euler solution of the maximum-flow operating point for this rotor. Good comparisons were found near the tip, but the computed shock structures at midspan and near the hub were incorrect. Bow waves were poorly resolved. Several improvements over reference 8 have been made in the present work. First, bow wave resolution has been improved by increasing the grid size and by clustering the grid around the leading edge. Second, shock structures have been improved by replacing measured exit hub static pressure input to the code with values calculated by using a two-dimensional through-flow code. The procedure used to calculate appropriate boundary values is described in detail later. Third, the near-stall results presented herein may be of more interest to designers since these results are more representative of a typical compressor design point. Finally, a film supplement (C-299) to this work uses computer animation to demonstrate convergence of the maximum-flow solution. The film also shows a time-accurate transition from the maximum-flow operating point to the near-stall operating point due to changes in boundary values. A request card and a description of this film are included at the back of this report.

Experimental Apparatus

Compressor Rotor

Rotor 33 was designed at the NASA Lewis Research Center as an inlet rotor for a core compressor. The flowpath consists of a constant-radius hub and a converging tip. At the inlet the tip radius is 254 mm (10 in.) and the hub-tip radius ratio is 0.7. The rotor has 52 blades with a tip chord of 44.5 mm (1.75 in.) and a tip solidity of 1.48. At the design speed of 16 100 rpm the tip speed is 426 m/sec (1398 ft/sec).

The rotor was tested without inlet guide vanes or stators, thereby eliminating any circumferential variations that would be introduced by stationary blade rows. Radial surveys of total pressure, total temperature, and flow angle were taken upstream and downstream of the blade row by using 6.4-mm-diameter combination probes each containing a thermocouple, a total pressure tube, and null-balancing static pressure holes. Radial surveys of static pressure were taken by using 6.4-mm-diameter wedge static probes. The upstream and downstream measurement stations, designated stations 1 and 2, were located one chord upstream and one-half chord downstream of the rotor, respectively. Details of the conventional probe survey and data reduction systems can be found in reference 2.

Data for this report were taken at design speed at two throttle settings, a wide-open, maximum-flow setting and a partially closed, near-stall setting. At maximum flow the rotor pressure ratio was 1.49 and the mass flow was 208 kg/(sec m^2) (42.40 lbm/(sec ft^2)). Mass flows were measured by using a calibrated orifice located far upstream and are accurate to within 1 percent. Inlet relative Mach numbers at maximum flow ranged from 1.14 near the hub to 1.35 near the tip. Near stall the rotor pressure ratio was 1.66 and the mass flow was 191 kg/(sec m^2) (39.12 lbm/(sec ft^2). Inlet relative Mach numbers near stall ranged from 1.05 near the hub to 1.32 near the tip.

Laser Anemometer

The fringe type of laser anemometer (LA), described in detail in reference 4 and shown schematically in figure 1, is a single-channel, dual-beam system with on-axis backscatter light collection. Laser light from a 1.6-W

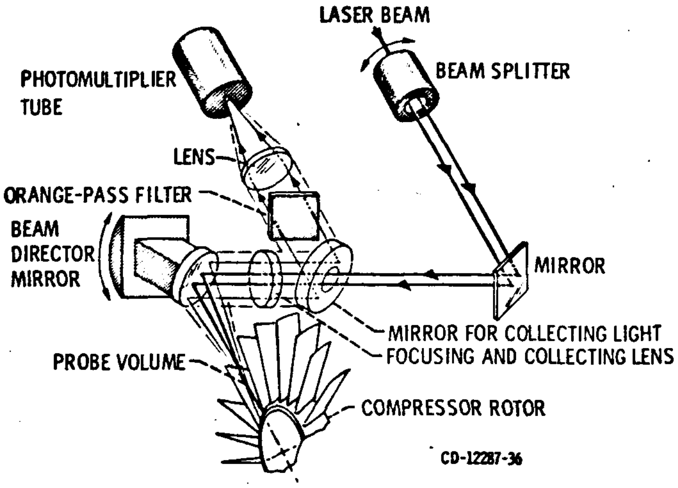

Figure 1. - Laser anemometer system optical layout.

argon ion laser that operates at a wavelength of 514.5 nm (visible green) is split into two parallel beams. A focusing lens causes the beams to cross at an angle of 2.825° at a selected point within the blade row, producing an interference fringe pattern with a spacing of 10.4 μm with a probe volume approximately 125 μm in diameter and 2 mm long. Light backscattered from seed particles injected upstream is collected through an 11° cone angle and focused onto a photomultiplier tube. The seed particle crossing frequency (which is proportional to the particle and flow velocity) is measured by a commercial LA processor. A dedicated minicomputer, a disk storage system, and a cathode-ray-tube (CRT) display were used for real-time data acquisition and processing. The minicomputer was also connected to a large central computer for additional data processing and graphical output. Velocity measurements made with the LA system are accurate to within 1 percent.

A window fabricated from commercial window glass provided optical access to the compressor. The window conformed to the outer endwall contour and measured 102 mm axially by 51 mm in circumference (11° arc) by 3 mm thick.

The entire optical system was mounted on an X-Y traversing table that was used to set the axial and radial positions of the probe volume. Axial and circumferential velocity components were resolved by rotating the beam splitter and hence the fringe pattern. The beam director mirror was used to move the beams away from the radial direction, providing access to regions normally shadowed by the blade tips and also providing limited capability of measuring radial velocities.

Seed particles consisted of spray-atomized rhodamine 6G dye dissolved in a solution of benzyl alcohol and ethylene glycol. The particles were injected into the flow 460 mm upstream of the rotor. When exposed to laser light, the seed particles fluoresce orange. An orange-pass optical filter placed in front of the photomultiplier selectively removed unwanted green laser light reflected from the hub and blades. The seed particle diameter was determined by equating the particle velocity lag measured downstream of the rotor passage shock to that predicted by a one-dimensional Stokes drag model and then solving for the unknown particle diameter. The particle diameter found by this procedure was 1.2 to 1.5 μm (ref. 5).

The angular position of a given measurement was determined by using a shaft angle counter that worked as follows: A once-per-revolution (OPR) signal was obtained from an optical sensor detecting a target on the rotating hub. A frequency synthesizer controlled by the minicomputer was used to produce a fixed-length pulse train relative to the OPR signal, regardless of the rotor speed (10 400 pulses per revolution, or 200 pulses per blade passage.) Frequency synthesizer pulses were counted by the shaft angle counter, which was reset to zero at each OPR signal. When a velocity measurement was made, the pulse count, which is a direct measure of the shaft angular position relative to the OPR target, was recorded with the velocity. The circumferential distance between measurement points varied from 0.43 mm at the hub to 0.61 mm at the tip.

An efficient data acquisition system made it possible to map the blade-to-blade distribution of a velocity component at a given axial and radial position very quickly. Whenever a seed particle crossed the probe volume, the particle velocity and the rotor shaft angular position were recorded as a data pair. Approximately 30 measurements were made at each of 1000 different shaft positions distributed as 50 positions per blade passage over 20 consecutive blade passages. The 30 velocities and flow angles at each shaft position were averaged to give time-averaged velocity distributions over 20 consecutive passages. The time-averaged distributions were analyzed to detect variations between individual passages. The results of this analysis are given in reference 5. The 20 time-averaged velocity distributions were then spatially averaged to yield the velocity distribution across an average passage. A typical run consisting of 30 000 measurements at a single axial and radial position took between 15 and 45 sec.

Errors in the LA measurements arise from a number of sources. The sources of error and the corresponding error magnitudes have been discussed in detail in reference 5 and are only summarized herein. Passage-to-passage velocity variations were of the order of 5 percent for most runs. Spatial averaging of data obtained across 20 blade passages improved the statistical accuracy of the data. Compressor speed drift during a run was of the order of 0.3 percent, and the repeatability of a given run was 1 percent. The error in velocity and flow angle measurements, which encompassed 95 percent of the data, was generally 5 percent or less except in regions immediately downstream of shocks, where seed particle velocity lag was the dominant error. The observed lag distance required for the seed particles to achieve 95 of the postshock gas velocity was found to be 13 t of chord for the maximum-flow case at 15 of span from the tip. The LA data have not been ed for particle lag since velocity variations due to lag cannot in general be distinguished from those o the compression process.

ure 2 shows the LA measurement stations and survey stations superimposed on the finite ence grid used with the three-dimensional code. ally 22 measurement stations lie along each of three n streamlines located at 15, 50, and 85 percent of rom the tip, with 12 of the axial stations inside the row. The three radial locations lie within 1 percent of the grid lines shown. At the near-stall operating LA measurements were taken only at 15 percent of from the tip.

nputational Methods

Dimensional Through-Flow Code MERIDL

through-flow analysis code used in the present is the MERIDL code described in reference 3. The solves an axisymmetric, inviscid momentum ion for a stream function along a midchannel, hub-ud stream surface. The stream function is defined to fy continuity identically and is differentiated erically to find individual velocity components. modynamic quantities are found from isentropic ons. Rotation, passage convergence, blade row ng, and blockage are all accounted for in the nulation. A successive-overrelaxation finite ence technique is used to solve the nonlinear stream tion equation. An orthogonal finite difference grid 10 points radially and 40 points axially (10 points eam and downstream, 20 within the blade row) was for the present calculations. Although the grid is not n here, it had the same extent as the three-nsional grid shown in figure 2. Input to MERIDL ts of blade, hub, and tip geometry, mass flow, eam total conditions, upstream and downstream whirl rV_θ distributions, and axial and radial distributions of total pressure loss. Upstream total conditions were input as constants radially and the upstream whirl was set to zero. The exit whirl was taken as a smooth curve fit through the measured probe data, excluding points obviously in the endwall boundary layers.

Three-Dimensional Euler Code BLADE3D

The three-dimensional analysis code used in the present work is the BLADE3D code described in reference 6. Only a brief description is given herein. The equations solved are the inviscid, unsteady Euler equations written in cylindrical coordinates. The equations include the continuity equation, the axial, radial, and circumferential momentum equations, and the energy equation, which are solved for the density, three velocity components, and the total energy. Pressure is found from the ideal-gas law. Blade row rotation is specified. Either a weak conservative or a nonconservative form of the equations can be solved. The nonconservative form was solved herein, implying that shock locations and jumps may be slightly in error.

MacCormack's explicit time-marching finite difference method in split operator form (ref. 19) is used to advance the unsteady solution in time from an initial guess to a converged steady solution. The method is second-order accurate and conditionally stable. Shocks are captured automatically and smeared over several grid points. Artificial viscosity terms are added to improve stability near shocks, but they also increase shock smearing.

Algebraic mappings are used to transform the complex flowpath geometry into a rectangular computational domain. The computational mesh had 100 axial points (32 points upstream and downstream and 34 within the blade), 17 circumferential points, and 18 radial points. Axially the grid points were clustered around the leading and trailing edges to improve the resolution of bow and shock waves. Points were stretched upstream and downstream to allow imposition of axisymmetric far-field conditions. Radially and circumferentially the points had constant spacing. A sheared blade-to-blade

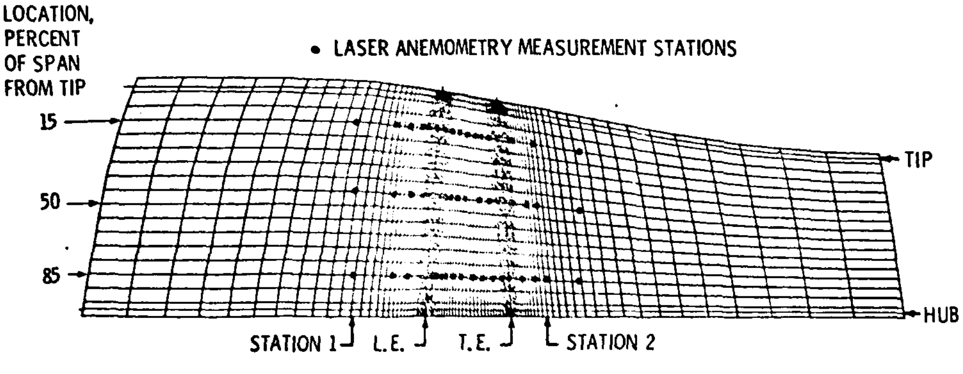

Figure 2. - Meridional view of computational grid showing laser anemometry measurement stations and conventional probe measurement stations.

grid was used. Figure 2 shows a meridional view of the grid, and figure 3 shows a blade-to-blade view near the hub, with upstream and downstream regions partially omitted.

At the inlet grid plane the flow is assumed to be axisymmetric and is matched to desired conditions at upstream infinity, where total conditions are specified, the radial velocity is zero, and the whirl is specified (here also zero.) The nonreflective inlet boundary condition is based on the one-dimensional method of characteristics. The desired axial velocity and static temperature at upstream infinity are combined to form a single variable, the value of the downstream-running characteristic. This value may be computed from the desired mass flow or the upstream Mach number, by using isentropic relations, or from MERIDL output. Although the BLADE3D solution is sensitive to the input characteristic value, all methods of computing that value give consistent results. The intersection of the specified downstream-running characteristic and the computed upstream-running characteristic at the inlet determine the inlet static temperature and axial velocity. The mass flow is computed as part of the solution and may not necessarily match the measured value.

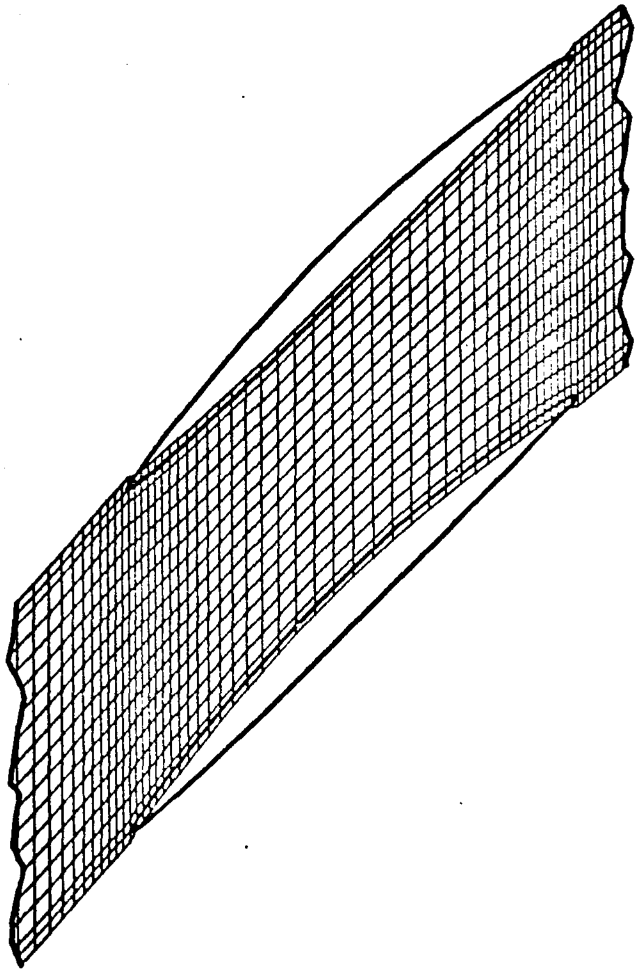

Figure 3. - Blade-to-blade view of computational grid 85 percent of span from tip. (Upstream and downstream regions omitted.)

At the exit grid plane the flow is also assumed to be axisymmetric, and the radial velocity is set to zero. The exit circumferential velocity, density, and downstream-running characteristic are extrapolated from within the flow field. Only one boundary value is specified, the hub static pressure at the exit of the computational domain. A radial equilibrium equation is integrated from hub to tip at the exit to determine the radial pressure distribution, which supplies the final unknown at the exit.

The specified upstream and downstream boundary conditions correspond to those conditions that an experimentalist can control. The upstream stagnation conditions correspond to plenum conditions, usually taken as standard atmospheric. The downstream pressure condition corresponds to a throttle setting that controls the blade row pressure ratio and mass flow.

Other boundary conditions used in the BLADE3D code include periodicity upstream and downstream of the blade row, tangency on the hub, shroud, and blade surfaces, and a Kutta condition specifying constant static pressure across the blade trailing edge.

Exit Pressure Specification

Euler codes typically require that the exit static pressure be specified as a boundary condition when the exit flow is subsonic. This input variable controls the computed mass flow and shock structure and must be specified correctly to produce reasonable solutions. Experience with the BLADE3D code has shown that using measured values of exit hub static pressures tends to produce solutions with higher mass flows and stronger shocks than those measured. This appears to be due to the neglect of viscous blockage and losses. Without these viscous effects, the BLADE3D code predicts higher mass flows for a given static pressure rise, or conversely, predicts a higher static pressure rise for a given mass flow than would be found in a viscous flow. Hence, to compute a case with a given mass flow, a designer must input an exit static pressure somewhat higher than measured. That exit pressure can be varied iteratively to match the desired mass flow, but computational times may become prohibitive.

Since the desired mass flow is an input variable for the MERIDL code and static pressures are included in the output, and since a MERIDL solution can be run in about 1 min of computer time, the MERIDL code can be used effectively to estimate exit hub static pressures for the BLADE3D code.

Measured values of mass flow, upstream total conditions, and inlet and exit whirl are input to MERIDL as described earlier. One piece of input remains to be described, the axial and radial distributions of total pressure loss. Since MERIDL is incapable of predicting either shock or viscous losses, the amount of loss specified can make a MERIDL solution compare well with either measured data or a BLADE3D solution. For best comparison with measured data, measured losses must be input. But for best comparison with a BLADE3D solution, only shock losses must be input.

Because the axial distribution of the loss has little or no effect on the exit static pressure, losses can be distributed evenly within the blade row. Radial distributions of shock losses in rotor 33 were calculated as part of the probe data reduction by using the Miller-Hartmann model described in reference 1. The model estimates shock losses to be those occurring across a single normal shock standing near the passage entrance. The Mach number ahead of the shock is taken as the average of the inlet relative Mach number and a somewhat higher value on the suction surface near the shock intersection.

At the near-stall operating point rotor 33 has a single-shock system like the one in the Miller-Hartmann model, but at the maximum-flow point it has a two-shock system that is not modeled correctly. Overall the BLADE3D near-stall solution compares better with the LA data than the maximum-flow solution does. Much of this is attributed to the better fit of the near-stall shock structure to the Miller-Hartmann model.

Computational Details

Initial conditions for the maximum-flow case assumed constant upstream velocity based on a specified inlet Mach number, velocity variations within the blade row based on blade turning, and constant velocity downstream. Solutions were run on an IBM 3030 computer. The time step used ranged from 75 to 90 percent of the stability limit. Convergence to a steady state was determined by monitoring the trailing-edge pressure distribution, which reflects the Kutta condition and the blade loading. Trailing-edge pressures were converged to the fourth significant figure.

The maximum-flow case took approximately 12 CPU hours (4500 time steps) to converge. The near-stall case was calculated as the time-accurate response of the maximum-flow case to a 9.6 percent increase in exit hub static pressure and a change in inlet conditions that resulted in an inlet Mach number drop of 0.06. The unsteady results are presented in the film supplement, which shows the transition of the shock system from one operating point to another. This case took nearly twice as long to converge as the maximum-flow case did because of the additional time necessary for the downstream pressure rise to travel upstream against a high subsonic flow. Starting from the nearly constant initial conditions described earlier, the near-stall case converges about as fast as the maximum-flow case. Thus, when only a steady solution is desired, it is often computationally more efficient to start with a simple initial guess than with a converged solution for a different flow.

The computer times quoted above are large. It should be noted that they were accumulated over many runs by restarting the code. Computer times can be reduced substantially by reducing grid size and grid clustering. The fine grid used here had 30 600 points. Solutions for the film supplement were run by using a coarser grid with 10 200 points in about 2 hours of computer time.

Comparisons between the fine-grid solutions presented later and the coarser-grid solutions generated for the film show that the coarser-grid solution reproduces all of the flow features of the fine-grid solution. Shocks tend to be smeared over five or six grid points on either grid, and consequently are smeared over a greater physical distance on the coarser grid. Coarse-grid solutions would appear to be useful to designers for analysis of preliminary designs, and fine-grid solutions for verification of final designs.

Film Supplement

A narrated, 16-mm color film supplement is available to illustrate the computations made with the BLADE3D code. A request card for ordering this film is included at the end of this report.

The film uses computer-animated contour plots of relative Mach number on a mean-flow stream surface near midchannel (like fig. 11 or 21) to demonstrate convergence of the maximum-flow solution and the unsteady transition to the near-stall operating point. In other sequences contour plots are swept across the passage to show the three-dimensional nature of the solution. Scenes of the laser anemometer test apparatus are also included. To save computer time, the grid used for the film had 60 axial, 10 radial, and 17 circumferential points – one-third as many points as the grid used for this report. On the coarse grid the maximum-flow case was calculated in 137 minutes, including the time needed to produce 560 contour plots. Again, the unsteady transition to near stall took about twice as long. Because the grid used for the film had a shorter axial extent than the grid used herein, the inlet characteristic values and the exit hub static pressures were interpolated from the fine grid onto the coarse grid to insure similarity between the two sets of solutions.

Results and Discussion

Near-Stall Operating Point

Since mass flow is computed by BLADE3D and pressure ratio is computed by both BLADE3D and MERIDL, these global parameters are of particular interest. Table I shows that for the near-stall case the mass flow calculated by BLADE3D is 1.5 percent lower than the measured orifice value. The calculated mass flow given herein resulted from using the exit pressure calculated by MERIDL as outlined earlier. Total pressure ratios calculated by MERIDL and BLADE3D are both 12.4 percent high, probably because of the neglect of viscous losses and blockage.

Radial distributions of circumferentially averaged total pressure and relative Mach number are compared with probe measurements upstream and downstream of the rotor in figures 4 and 5. Probe measurement locations labeled station 1 and station 2 are indicated on figure 2. Upstream (station 1) the calculations and measurements are in good agreement. Downstream (station 2) the high total pressures calculated inviscidly are evident.

Axial distributions of relative Mach number and flow angle at 15 percent of span from the tip are compared in figures 6 and 7. The MERIDL calculations are, of course, axisymmetric. The BLADE3D and LA results are shown along a midgap line. In figure 6 the BLADE3D Mach numbers show good agreement with the LA measurements in the strong bow wave system and in the location of the passage shock. The passage shock jump is overpredicted, possibly because of the neglect of viscous blockage. Discrepancies between the shock jumps shown

TABLE I. - COMPARISON OF MEASURED AND CALCULATED MASS FLOWS AND TOTAL PRESSURE RATIOS - NEAR-STALL POINT

	Mass flow, $\dot{m}$		Total pressure ratio
	kg/(sec m^2)	lb/(sec ft^2)	
Laser anemometry	191	39.1	1.66
BLADE3D code	188	38.5	1.866
MERIDL code	[a]191	[a]39.1	1.864

[a] Mass flow is set explicitly as an input to MERIDL.

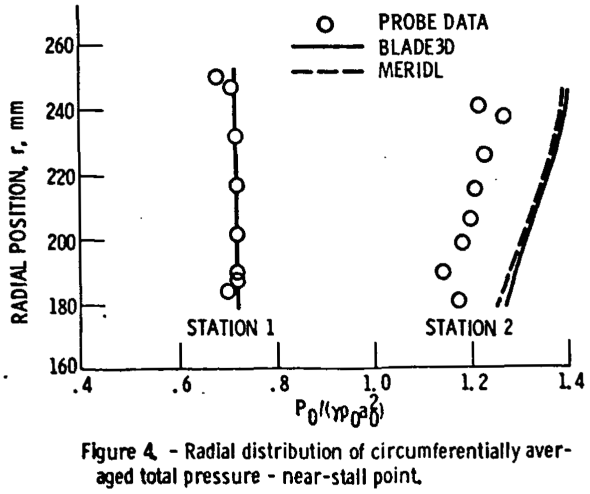

Figure 4. - Radial distribution of circumferentially averaged total pressure - near-stall point.

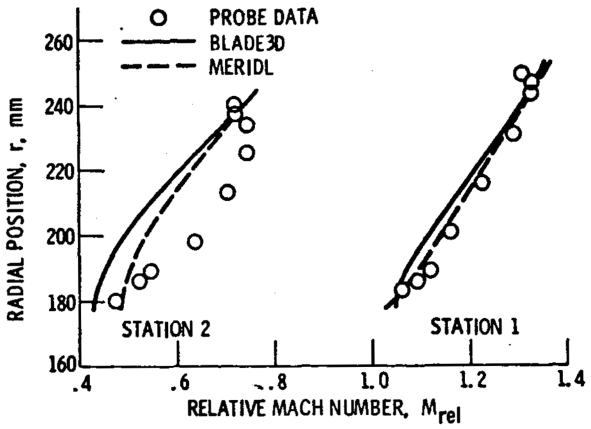

Figure 5. - Radial position of circumferentially averaged relative Mach number - near-stall point.

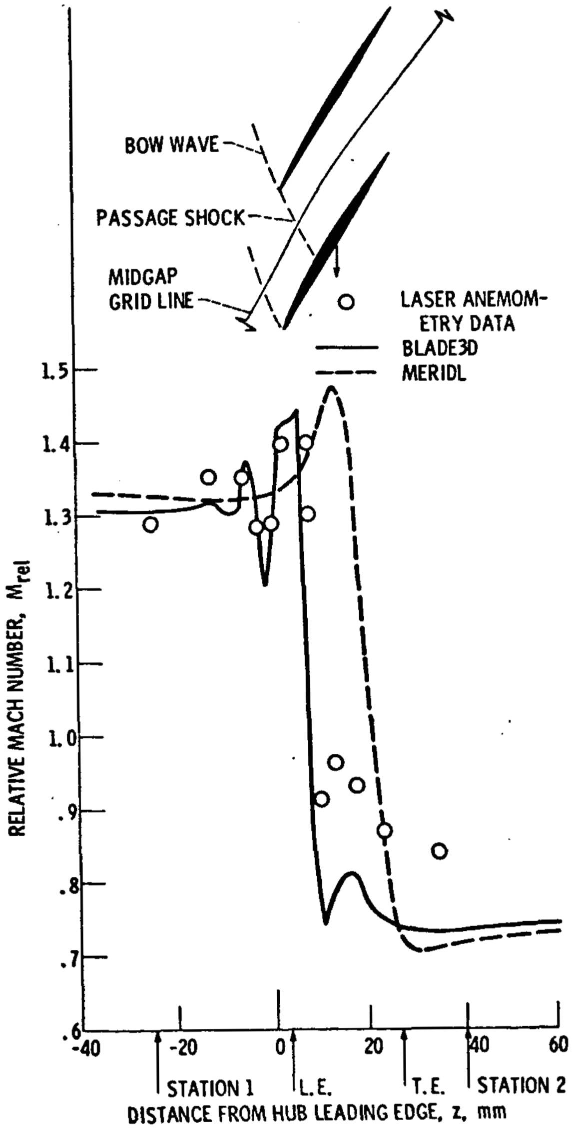

Figure 6. - Axial distribution of relative Mach number 15 percent of span from tip at midgap - near-stall point

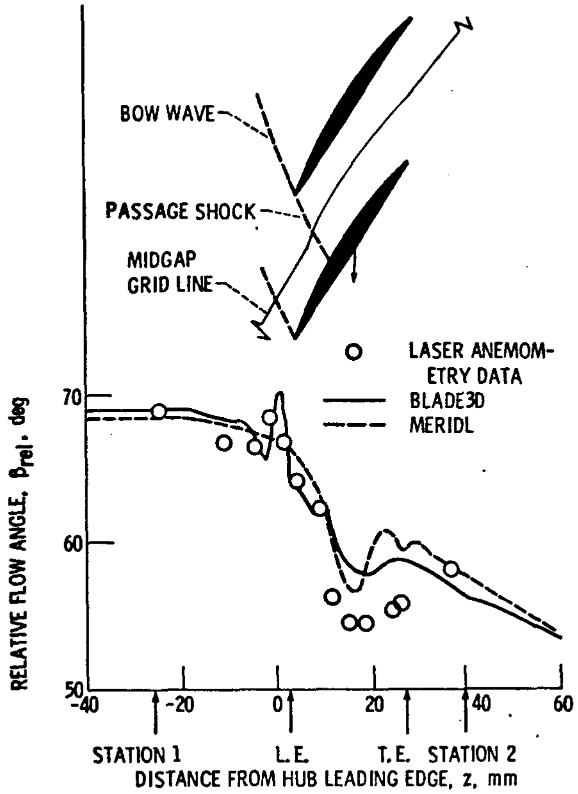

Figure 7. - Axial distribution of blade-to-blade relative flow angle 15 percent of span from tip at midgap - near-stall point.

and those obtained from the normal shock tables are due to inclination of the shock relative to the line along which the results are shown. The MERIDL results show an initial acceleration due to blockage followed by a rapid compression due to turning. MERIDL cannot capture the upstream wave system or the passage shock, yet the MERIDL results agree fairly well outside the blade row. In figure 7, BLADE3D captures the upstream wave system flow angles quite well, and MERIDL predicts a reasonable average flow. The BLADE3D and LA flow angles behind the shock disagree because of the disagreement in axial velocity components due to viscous effects.

Circumferential distributions of relative Mach number and flow angle at 15 percent of span from the tip and at 23 percent of chord (through the passage shock) are shown in figures 8 and 9. The abscissae of the plots showing percent gap are measured from the suction surface of a leading blade to the suction surface of the following blade. At this axial location the flow near the suction surface (left) is upstream of the passage shock, but the flow near the pressure surface (right) has passed through the shock. In figure 8 the shock location is clearly defined in both the LA measurements and the BLADE3D calculations as an abrupt drop in Mach number near midgap. The shock smearing evident in the LA measurements is due to seed particle lag, and the shock smearing in the BLADE3D calculations is due to artificial viscosity. MERIDL results agree with flow conditions on the upstream side of the shock. Relative flow angles shown in figure 9 are in reasonable agreement. MERIDL results are omitted from the remaining near-stall results.

Blade surface relative Mach number distributions along a design streamline at 15 percent of span from the tip are shown in figure 10. LA measurements of surface

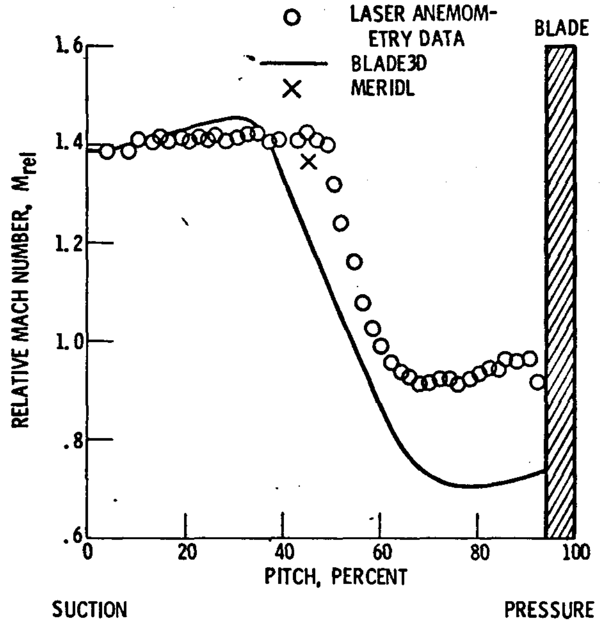

Figure 8. - Circumferential distribution of relative Mach number 15 percent of span from tip at 23 percent of chord (through passage shock) - near-stall point.

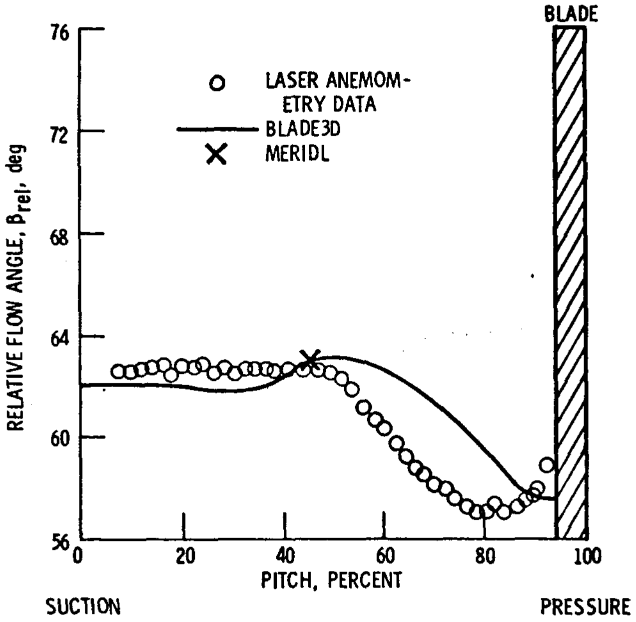

Figure 9. - Circumferential distribution of blade-to-blade relative flow angle 15 percent of span from tip at 23 percent of chord (through passage shock) - near-stall point.

relative Mach number were taken from plots like figure 8 as the first circumferential point for which a statistically significant number of measurements were taken (at least 20 measurements). At a tip chord Reynolds number of about 6×10^5, an unseparated turbulent blade boundary layer thickness would be of the order of the measurement point spacing; so it is felt that the first statistically significant measurement point should be near the edge of the core flow. Nevertheless, viscous effects may be present in the data. Suction-surface shock locations agree to within the measurement spacing. Both calculations and measurements show a forward blade loading.

Figure 11 shows contours of computed relative Mach number on a mean-flow surface at midchannel and is included to show the three-dimensional nature of the solution. Most of the upstream and downstream regions have been omitted. Dashed lines indicate shocks.

The shock structure at 15 percent of span from the tip is shown in figures 12 and 13, which compare computed and measured contours of relative Mach numbers and flow angles. Again, shocks are shown by dashed lines. Computed shock locations were determined from axial plots like figure 6 as grid points with maximum Mach numbers before a rapid drop. These grid points were located on the blade-to-blade plots and fit with smooth curves. Experimental shock locations were determined similarly except that circumferential plots like figure 8 were used. Figure 12 shows a pronounced bow wave and passage shock system with excellent agreement between the BLADE3D and LA results. Computed relative Mach numbers leaving the shock are low, however. The wakelike contours leaving the trailing edges in the computed results show an inviscid trailing-edge slip line. Relative flow angle contours in figure 13 show an upstream angle of 68° to 69°. The suction-surface metal angle at the leading edge is about 64°. The high-incidence incoming flow turns smoothly through expansion fans originating one or two blades away to become well aligned with the suction surface at the leading edge.

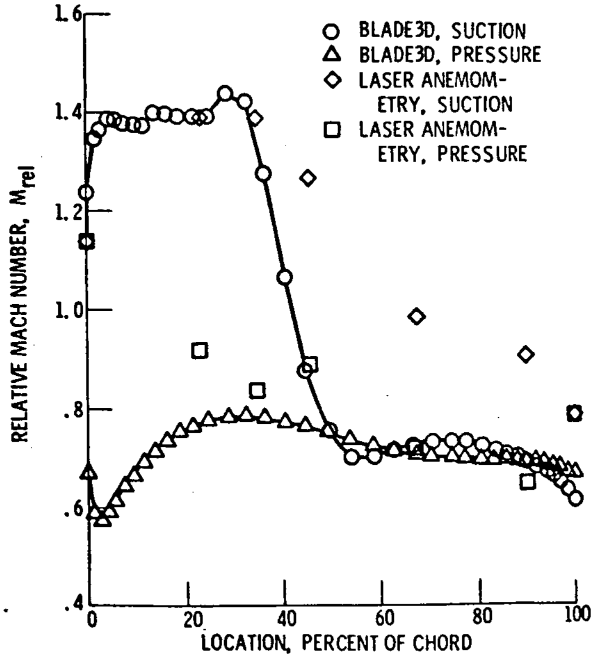

Figure 10. - Axial distribution of relative Mach number on blade surfaces 15 percent of span from tip - near-stall point.

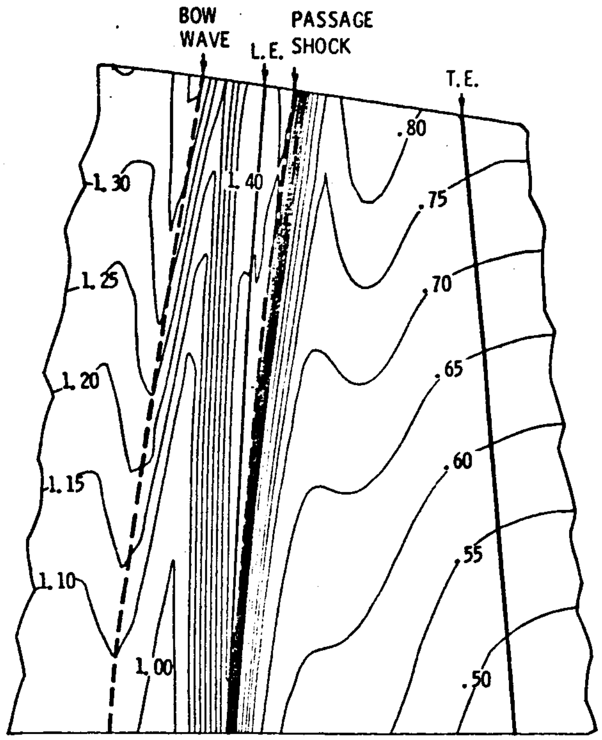

Figure 11. - Computed relative Mach number contours on mean-flow stream surface at midchannel - near-stall point.

Shock angles and a total pressure loss coefficient for the passage shock at midgap are tabulated in table II. The shock inclination angle α is measured from the axial direction. The shock loss coefficient is defined in equation (1) as

$$\omega_s = \frac{(1 - P_2/P_1)}{(1 - p_1/P_1)} \qquad (1)$$

where P and p refer to total and static pressure, respectively. The total pressure ratio P_2/P_1 is obtained from the normal shock relations by using the component of relative Mach number ahead of and normal to the shock. Since the passage shock is well defined in this case, the shock location and angle are relatively easy to determine. Slight discrepancies in flow conditions ahead of the shock account for a small disagreement in the shock loss parameters.

Maximum-Flow Operating Point

Mass flows and total pressure ratios for the maximum-flow case are compared in table III. The BLADE3D mass

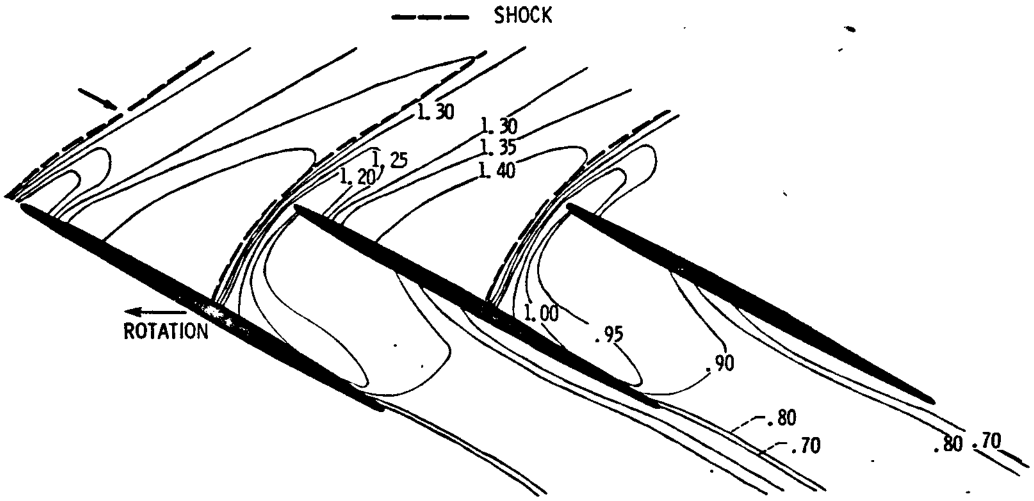

(a) Laser anemometry data.

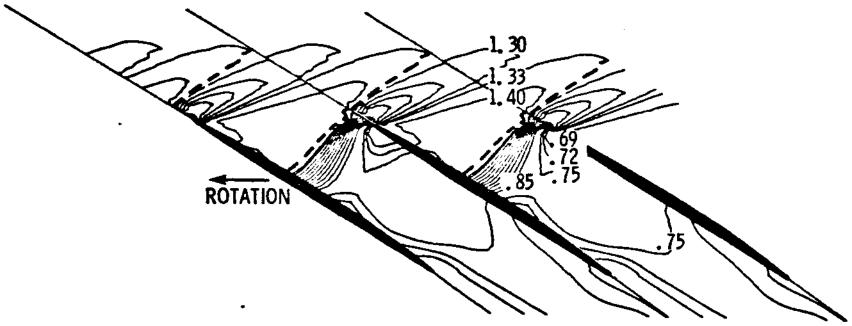

(b) BLADE3D calculations.

Figure 12. - Blade-to-blade contours of relative Mach number 15 percent of span from tip - near-stall point.

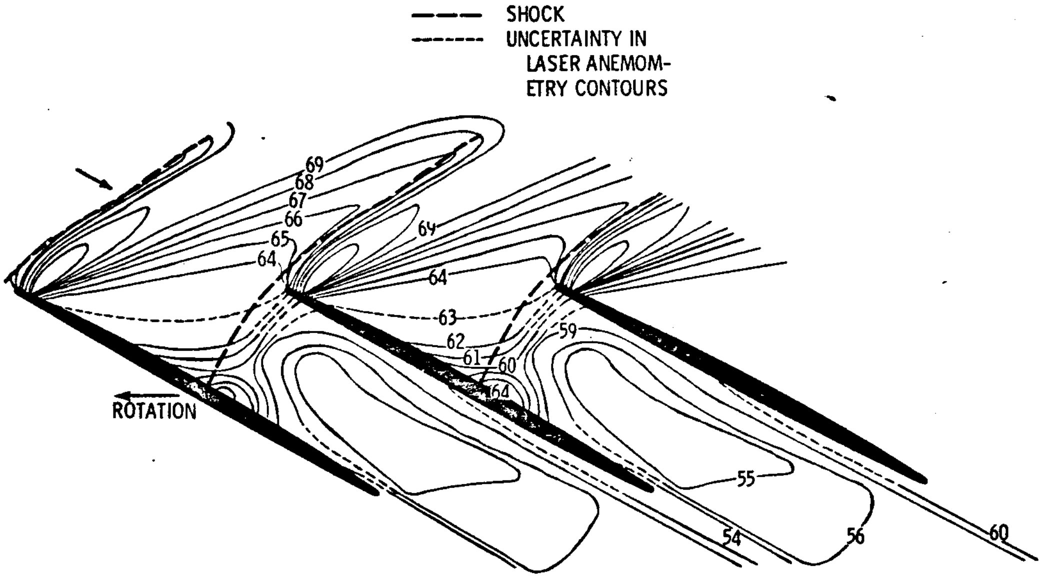

(a) Laser anemometry data.

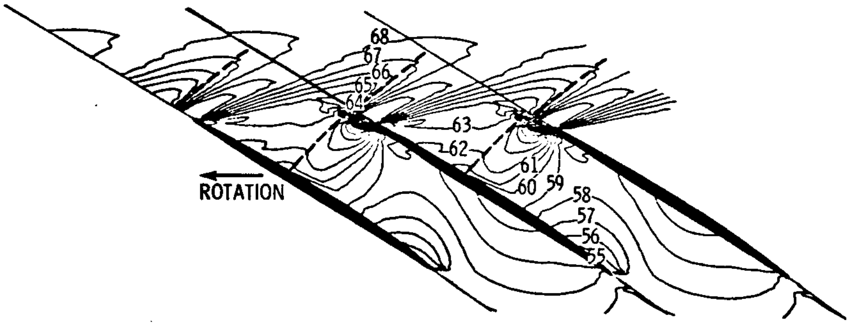

(b) BLADE3D calculations.

Figure 13. - Blade-to-blade contours of relative flow angle 15 percent of span from tip - near-stall point.

TABLE II. - COMPARISON OF MEASURED AND CALCULATED SHOCK LOSS PARAMETERS FOR PASSAGE SHOCK AT MIDGAP - NEAR-STALL POINT

[Location, 15 percent of span from tip.]

	Laser anemometry	BLADE3D program
Relative Mach number, M_{rel}	1.40	1.45
Relative flow angle, β_{rel}	62.5	62.1
Shock inclination angle, α	28.0	28.0
Shock loss coefficient, ω_s	0.061	0.078

TABLE III. - COMPARISON OF MEASURED AND COMPUTED MASS FLOWS AND TOTAL PRESSURE RATIOS - MAXIMUM FLOW POINT

	Mass flow, $\dot{m}$		Total pressure ratio
	kg/(sec m^2)	lb/(sec ft^2)	
Laser anemometry	208	42.1	1.49
BLADE3D code	218	44.6	1.71
MERIDL code	^{a}208	^{a}42.6	1.64

[a] Mass flow is set explicitly as an input to MERIDL.

flow is 4.8 percent higher than the measured orifice value. This is a substantial error at this operating point. Nevertheless, other aspects of the BLADE3D solution agree reasonably well with the LA data. Total pressure ratios calculated by both codes are high; BLADE3D is 14.8 percent high and MERIDL is 10.0 percent high. Differences between the BLADE3D and MERIDL solutions are attributed to differences in shock losses as calculated by BLADE3D and by the Miller-Hartmann model.

Radial distributions of circumferentially averaged total pressure and relative Mach number shown in figures 14 and 15 are similar to the near-stall results except for some disagreement between BLADE3D and MERIDL because of the BLADE3D mass flow error. Endwall boundary layer effects that cannot be predicted inviscidly are evident in the probe measurements, especially in the relative Mach number measurements near the tip of station 2.

Axial distributions of relative Mach number and flow angle are shown in figures 16 and 17. In figure 16 the MERIDL results show little upstream influence of the blades, while the BLADE3D and LA results show relative Mach number fluctuations due to a bow wave system. The computed bow wave is weaker than that measured. Within the blade row the measured and BLADE3D computed flows accelerate slightly, decelerate across an oblique passage shock, and finally decelerate sharply across a normal shock near the trailing edge. The MERIDL results show surprising agreement inside the blade row, but the agreement is coincidental. The initial acceleration in the MERIDL results is due to blade blockage. The rapid deceleration that appears to be a shock is due to rapid turning of the flow to match the specified downstream whirl. Downstream of the blade row both computed flows reaccelerate slightly because of tip convergence. Blade-to-blade relative flow angle results in figure 17 show the same trends as the relative Mach number. Agreement between computed and measured angles is good to midchord. Beyond midchord the computed axial velocity components are lower than those measured, causing the computed angles to be higher than those measured.

Circumferential distributions of relative Mach number and flow angle at 78 percent of chord (through the rear shock) are shown in figures 18 and 19. The Mach number distributions in figure 18 only agree qualitatively, with

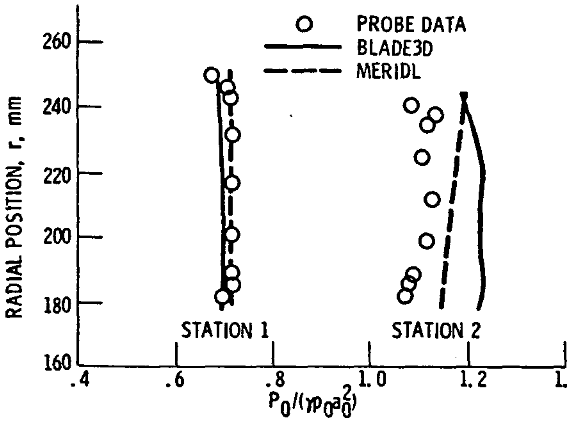

Figure 14. - Radial distribution of circumferentially averaged total pressure - maximum-flow point.

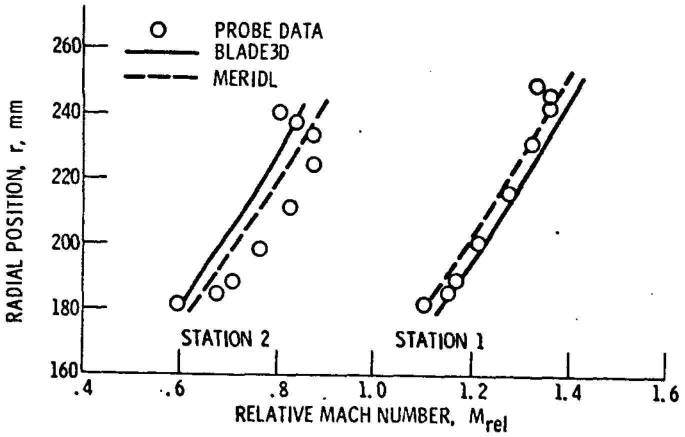

Figure 15. - Radial distribution of circumferentially averaged relative Mach number - maximum-flow point.

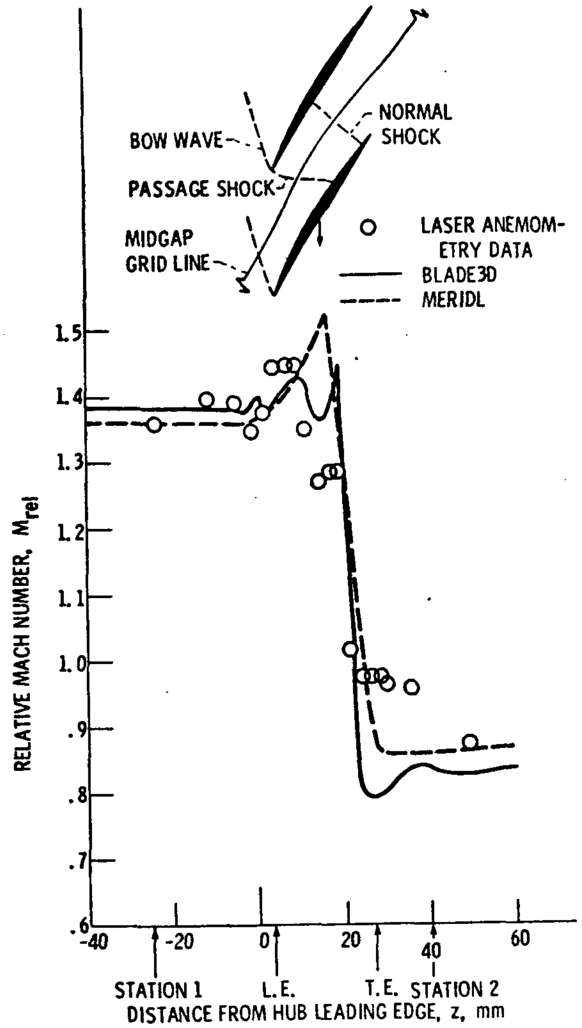

Figure 16. - Axial distribution of relative Mach number 15 percent of span from tip at midgap - maximum-flow point.

discrepancies in shock location and strength. At this axial location the flow near the suction surface (left) is upstream of the rear shock, but the flow near the pressure surface (right) has passed through the shock. It is possible that the measured dropoff in Mach number near the pressure surface is caused by shock-boundary layer interaction. MERIDL results look reasonable as an axisymmetric average. Relative flow angles in figure 19 compare similarly, except that the MERIDL result is high. MERIDL results are omitted from the remaining maximum-flow results.

Figure 20 compares computed and measured blade surface relative Mach numbers. The computations and measurements show qualitative agreement in shock location. They also show a dramatic shift of the blade loading to the rear as compared with the near-stall results in figure 10.

Computed relative Mach number contours on a midchannel mean-flow surface in figure 21 show a complete change in shock structure from the near-stall

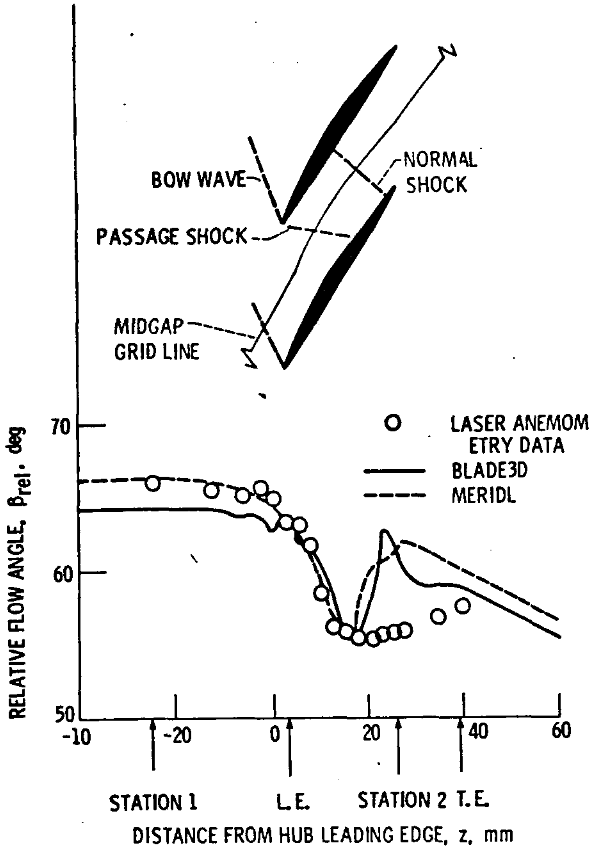

Figure 17. - Axial distribution of blade-to-blade relative flow angle 15 percent of span from tip - maximum-flow point.

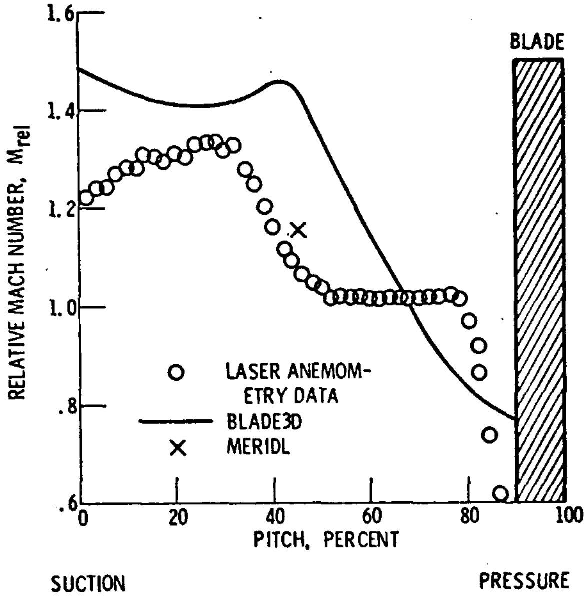

Figure 18. - Circumferential distribution of relative Mach number 15 percent of span from tip at 78 percent of chord (through rear shock) - maximum-flow point.

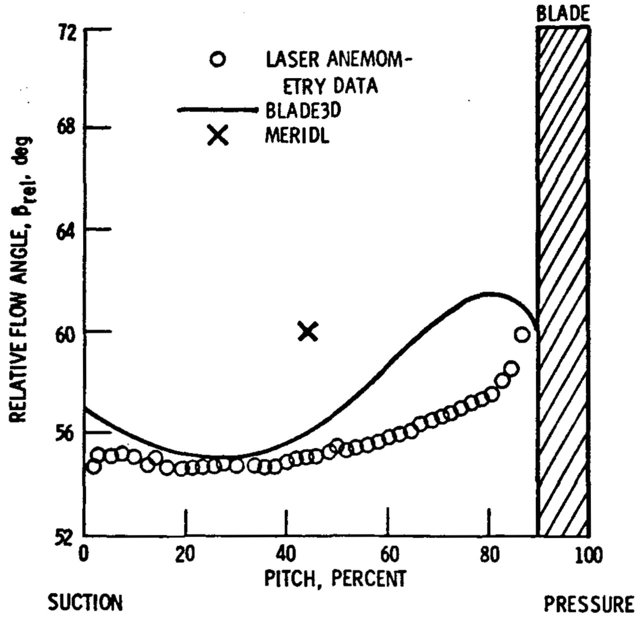

Figure 19. - Circumferential distribution of blade-to-blade relative flow angle 15 percent of span from tip at 78 percent of chord (through rear shock) - maximum-flow point.

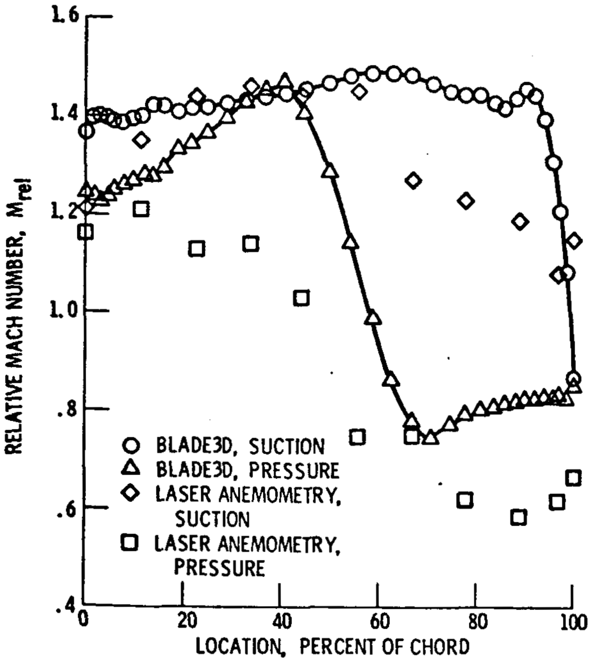

Figure 20. - Axial distribution of relative Mach number on blade surfaces 15 percent of span from tip - maximum-flow point.

solution in figure 11. In the maximum-flow solution the bow wave and passage shock are weaker than in the near-stall solution. The rear passage shock is slightly curved from hub to tip. Near the hub it is difficult to distinguish whether there is a rear shock or just a diffuse compression.

Computed and measured blade-to-blade relative Mach number contours are compared side-by-side at the three

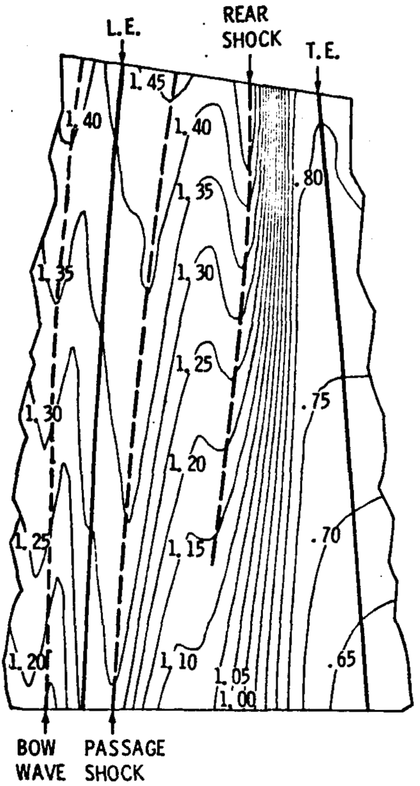

Figure 21. - Computed relative Mach number contours on mean-flow surface at midchannel - maximum-flow point.

spanwise locations in figure 22. At 85 percent of span from the tip the computations and measurements are in excellent agreement. Both show a bow wave with an exit Mach number of 1.2. The calculations show a stronger suction-surface acceleration than the data. Both show a forward passage shock with similar exit Mach numbers and small sonic regions on the pressure surface near the leading edge. Finally both show a diffuse compression to subsonic with no obvious rear shock. The calculated flow exits at a considerably lower Mach number than the measured flow. At midspan the comparison is similar except that here both show a definite rear shock. The measured rear shock is forward in the passage relative to the calculated shock and may even be a reflection of the front shock. At 15 percent of span from the tip the LA measurements show a stronger bow wave and passage shock than the BLADE3D solution. The calculations and measurements both show very strong rear shocks attached to the trailing edge. These results show improved bow wave resolution and rear shock location over the results in reference 8 because of grid refinement and adjustment of the exit hub static pressure.

Contour plots of blade-to-blade relative flow angle at midspan are compared in figure 23, with the shock locations from figure 22 indicated. The measured and computed contours are similar but difficult to compare. A periodic upstream angle variation of about 1° was measured but was not computed. One note of interest is

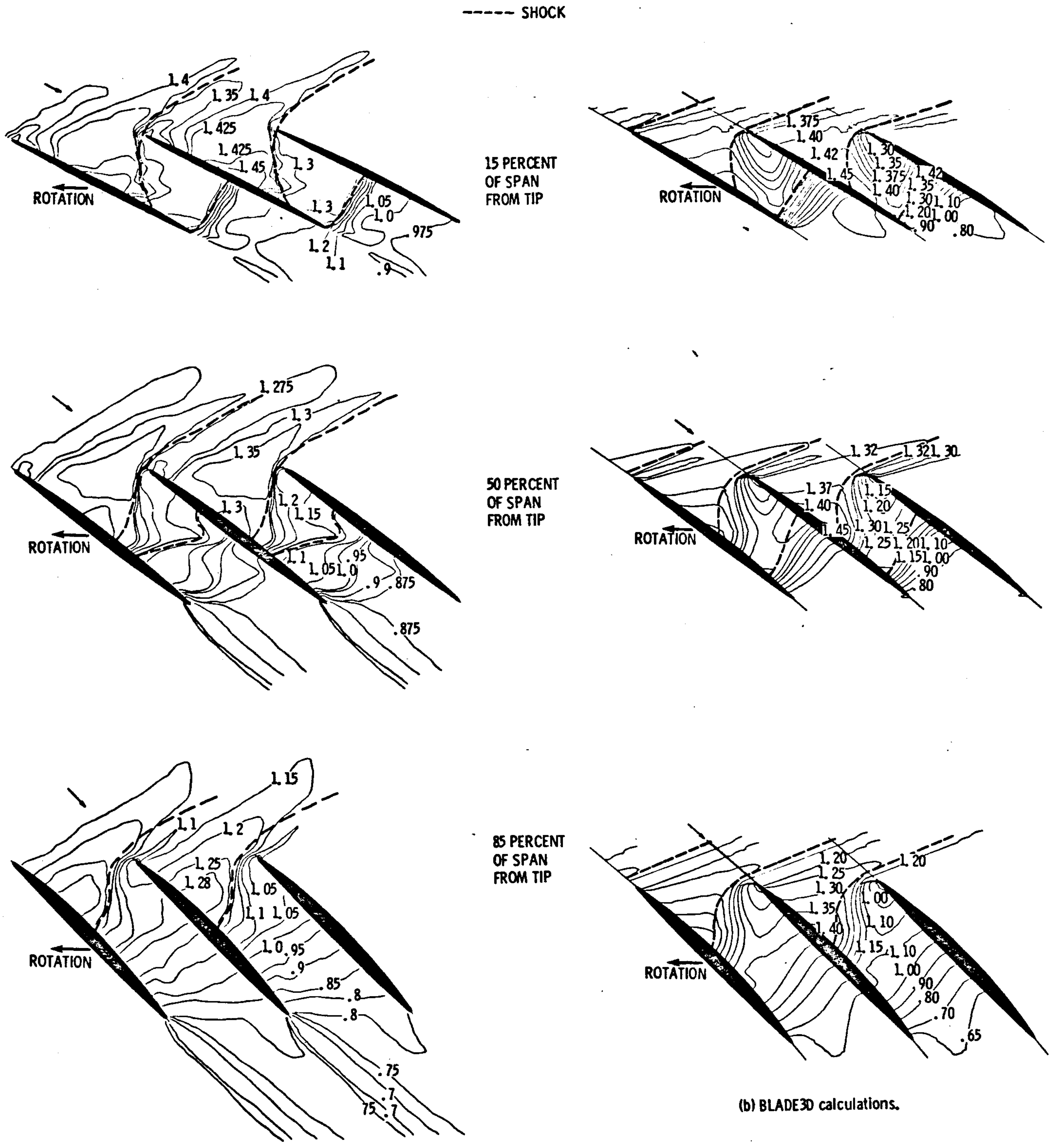

(b) BLADE3D calculations.

(a) Laser anemometry data.

Figure 22. - Blade-to-blade contours of relative Mach number - maximum-flow point.

TABLE IV. - COMPARISON OF MEASURED AND CALCULATED SHOCK LOSS PARAMETERS FOR REAR SHOCK AT MIDGAP - MAXIMUM-FLOW POINT

	Laser anemometry			BLADE3D code		
	Location, percent of span from tip					
	15	50	85	15	50	85
Relative Mach number, M_{rel}	1.28	1.37	1.45	1.32	1.39	1.43
Relative flow angle, β_{rel}	52.0	56.8	61.6	50.5	56.0	60.9
Shock inclination angle, α	10	5	0	14	7	2
Shock loss coefficient, ω_s	.004	.012	.024	.010	.016	.023

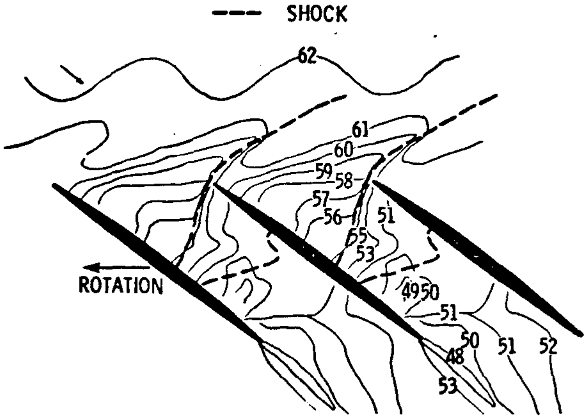

(a) Laser anemometry data.

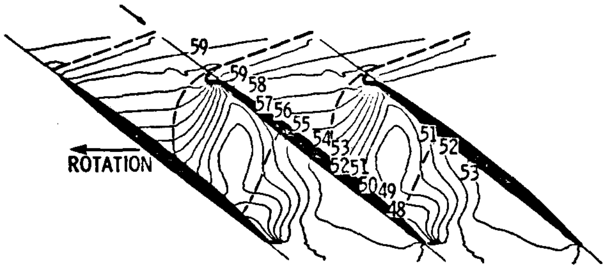

(b) BLADE3D calculations.

Figure 23. - Blade-to-blade contours of relative flow angle 50 percent of span from tip - maximum-flow point.

that flow angle contours do not always show shock locations.

Table IV compares the measured and computed shock loss parameters at midgap and three spanwise locations. There is some disagreement between the LA and BLADE3D shock loss coefficients, especially at the hub. Part of the disagreement is due to small discrepancies ahead of the shock; part is due to shock inclination in the meridional plane; but most is due to difficulties in determining the shock angle from shock locations found, as described earlier.

Concluding Remarks

The laser anemometer (LA) system described is a highly time-efficient means of measuring flow velocity and angle in a rotating compressor. The use of a dedicated minicomputer for control of the LA system and for data acquisition and processing was responsible for the efficiency of the system. Current LA measurements are of sufficient accuracy for verification of inviscid codes. Shock smearing in the LA measurements due to seed particle lag is of roughly the same magnitude as numerical shock smearing, and both need to be reduced. Either a better method of estimating boundary layer edge velocities or a means of directly measuring blade surface pressures is needed. More detailed measurements of blade and endwall boundary layers will be needed for verification of viscous codes.

Inviscid calculations from an axisymmetric throughflow code (MERIDL) and a three-dimensional Euler code (BLADE3D) compare well with probe data upstream of the blade row. Downstream, total pressures are high and relative Mach numbers are low because viscous effects are neglected. Within the blade row the axisymmetric solutions agree only qualitatively with the other results.

The BLADE3D code accurately predicted Mach number and flow angle distributions and shock structure within an axial compressor rotor at maximum-flow and near-stall operating points. The near-stall solution agrees better with LA measurements than the maximum-flow solution does. This is probably because most of the flow turning in the near-stall case occurs across a forward passage shock away from viscous effects. But in the maximum-flow case a second normal shock near the blade trailing edge (where viscous effects would be greatest) controls the blade row pressure rise. Present results for the maximum-flow case have improved on earlier results presented by the authors. Bow wave resolution was improved through grid clustering, and rear shock structure was improved by adjusting the exit hub static pressure.

Downstream pressure boundary conditions typically needed by Euler codes are difficult to specify. Measured downstream pressures produce erroneous mass flows and shock structures because measured pressures contain viscous losses not accounted for in inviscid codes. Computational times may prohibit iterating on boundary conditions. An axisymmetric through-flow code like MERIDL can be used as a consistent and computationally efficient tool for choosing downstream boundary values. MERIDL input includes total conditions, mass flow, and upstream and downstream whirl – all input as measured. Shock losses must be specified and can be estimated by using the Miller-Hartmann model along with measured probe data. Loss distribution through the blade row does not significantly affect the computed upstream or downstream solution. Downstream pressures calculated in this manner are higher than measured pressures but are appropriate boundary values for Euler codes, producing the best agreement between mass flows and shock structures measured in a viscous flow and computed inviscidly. In future three-dimensional viscous codes the measured downstream pressure should suffice.

A narrated, 16-mm color film is available to illustrate the LA system and calculations made with the BLADE3D code. Mach number contour plots at midgap generated at successive time steps show the convergence of the maximum-flow solution. Unsteady transition from the maximum-flow point to the near-stall point is calculated as a result of changes in boundary conditions. Other sequences show the three-dimensional solution by sweeping contour viewing planes through the flow field in the three coordinate directions.

Lewis Research Center
National Aeronautics and Space Administration
Cleveland, Ohio, January 27, 1982

References

1. Miller, G. R.; Hartmann, M. J.: Experimental Shock Configuration and Shock Losses in a Transonic Compressor Rotor at Design Speed. NACA RM E58A14b, 1958.
2. Moore, R. D.; Lewis, G. W., Jr.; and Osborn, W. M.: Performance of a Transonic Fan Stage Design for a Low Meridional Velocity Ratio. NASA TP-1298, 1978.
3. Katsanis, T.; and McNally, W. D.: Revised FORTRAN Program for Calculating Velocities and Streamlines on the Hub-Shroud Midchannel Stream Surface of an Axial-, Radial-, or Mixed-Flow Turbomachine or Annular Duct. I – Users Manual. NASA TN D-8430, 1977.
4. Powell, J. A.; Strazisar, A. J.; and Seasholtz, R. G.: Efficient Laser Anemometer for Intra-Rotor Flow Mapping in Turbomachinery. J. Eng. Power, vol. 103, no. 2, Apr. 1981, pp. 424–429.
5. Strazisar, A. J.; and Powell, J. A.: Laser Anemometer Measurements In a Transonic Axial Flow Compressor Rotor. J. Eng. Power, vol. 103, no. 2, Apr. 1981, pp. 430–437.
6. Thompkins, W. T., Jr.: A FORTRAN Program for Calculating Three-Dimensional Inviscid Rotational Flows with Shock Waves in Axial Compressor Rotors. NASA CR-3560, 1982.
7. Steger, J. L.; Pulliam, T. H.; and Chima, R. V.: An Implicit Finite Difference Code for Inviscid and Viscous Cascade Flow. AIAA Paper 80-1427, July 1980.
8. Strazisar, A. J.; and Chima, R. V.: Comparison Between Optical Measurements and a Numerical Solution of the Flow Field Within a Transonic Axial-Flow Compressor Rotor. AIAA Paper 80-1078, June 1980.
9. Epstein, A. H.: Quantitative Density Visualization in a Transonic Compressor Rotor. J. Eng. Power, vol. 99, no. 3, July 1977, pp. 460–474.
10. Schodl, R.: A Laser Dual-Beam Method for Flow Measurements in Turbomachines. ASME Paper 74-GT-157, March 1974.
11. Schodl, R.: A Laser-Two-Focus (L2F) Velocimeter for Automatic Flow Vector Measurements in the Rotating Components of Turbomachines. Measurement Methods in Rotating Components of Turbomachinery, B. Lakshminarayana and P. Runstadler, Jr., eds., ASME, 1980, pp. 139–147.
12. Dunker, R. J.; Strinning, P. E.; and Weyer, H. B.: Experimental Study of the Flow Field Within a Transonic Axial Compressor Rotor by Laser Velocimetry and Comparison with Through-Flow Calculations. J. Eng. Power, vol. 100, no. 2, Apr. 1978, pp. 279–286.
13. Dunker, R. J.; and Strinning, P. E.: Flow Velocity Measurements Inside of a Transonic Axial Compressor Rotor by Means of an Optical Technique and Compared with Blade-to-Blade Calculations. Third International Symposium on Airbreathing Engines, Dietmar K. Hennecke and G. Winterfield, eds., DGLR-Fachbuchreihe Band 6, Munich, Germany, 1976, pp. 217–232.
14. Smart, A. E.; Wisler, D. C.; and Mayo, W. T., Jr.: Optical Advances in Laser Transit Anemometry. J. Eng. Power, vol. 103, no. 2, Apr. 1981, pp. 438–444.
15. Wisler, D. C.: Shock Wave and Flow Velocity Measurements in a High Speed Fan Rotor Using the Laser Velocimeter. ASME Paper 76-GT-49, Mar. 1976.
16. McDonald, P. W.; et al.: A Comparison Between Measured and Computed Flow Fields in a Transonic Compressor Rotor. ASME Paper 80-GT-7, Mar. 1980.
17. Denton, J. D.; and Singh, U. K.: Time Marching Methods for Turbomachinery Flow Calculations. Part I: Basic Principles and Two-dimensional Applications. Part II: Three-Dimensional Flows. In Application of Numerical Methods to Flow Calculations in Turbomachines, Lecture Series 1979-7, Von Karman Institute for Fluid Dynamics (Rhode Saint Genese, Belgium), 1979, p. 1–47.
18. Haymann-Haber, G.; and Thompkins, W. T., Jr.: Comparison of Experimental and Computational Shock Structure in a Transonic Compressor Rotor. J. Eng. Power, vol. 103, no. 1, Jan. 1981, pp. 78–88.
19. MacCormack, R. W.; and Paullay, A. J.: Computational Efficiency Achieved by Time Splitting of Finite Difference Operators. AIAA Paper 72-154, Jan. 1972.

Lewis motion-picture film supplement C-299 is available on loan. Requests will be filled in the order received.

The film (16 mm, 10 min, color, sound) shows a transonic compressor rotor, designated rotor 33, that has been studied experimentally by using laser anemometry and computationally by using the BLADE3D computer code. Details of the laser anemometer system and experimental test cell are shown. Computer animation illustrates computations made with the BLADE3D code. The code calculates three-dimensional inviscid flows in axial compressors by using a time-marching finite difference method. Colored contour plots made at successive times show the development of a steady-state solution and unsteady shock wave movement in response to changes in back pressure. Other sequences show the three-dimensional solution by sweeping the contour-viewing plane through the blade row in different directions. Narration and artwork are used to explain each sequence. Calculations like those presented in this film will be used heavily in the future to reduce costly wind tunnel testing of transonic compressor rotors. This film will be useful for explaining these calculations to potential users of the BLADE3D code.

Requests for film supplement C-299 should be addressed to

NASA Lewis Research Center
Attn: Chief, Management Services Division (5-5)
21000 Brookpark Road
Cleveland, OH 44135

cut

Date ____________________

Please send, on loan, copy of film supplement C-299 to TP-1931

Name of Organization

Street Number

City and State Zip Code

Attention: Mr. ____________________

Title ____________________

1. Report No. NASA TP-1931	2. Government Accession No.	3. Recipient's Catalog No.
4. Title and Subtitle COMPARISON OF TWO- AND THREE-DIMENSIONAL FLOW COMPUTATIONS WITH LASER ANEMOMETER MEASUREMENTS IN A TRANSONIC COMPRESSOR ROTOR		5. Report Date September 1982 6. Performing Organization Code 505-32-52
7. Author(s) Rodrick V. Chima and Anthony J. Strazisar		8. Performing Organization Report No. E-1007 10. Work Unit No.
9. Performing Organization Name and Address National Aeronautics and Space Administration Lewis Research Center Cleveland, Ohio 44135		11. Contract or Grant No. 13. Type of Report and Period Covered Technical Paper
12. Sponsoring Agency Name and Address National Aeronautics and Space Administration Washington, D.C. 20546		14. Sponsoring Agency Code

15. Supplementary Notes

Film supplement C-299 available on request. Presented in part at ASME Twenty-Seventh International Gas Turbine Conference, London, England, April 18-22, 1982 (NASA TM-82777).

16. Abstract

Two- and three-dimensional inviscid solutions for the flow in a transonic axial compressor rotor at design speed are compared with probe and laser anemometer measurements at near-stall and maximum-flow operating points. Experimental details of the laser anemometer system and computational details of the two-dimensional axisymmetric code and three-dimensional Euler code are described. Comparisons are made between relative Mach number and flow angle contours, shock location, and shock strength. A procedure for using an efficient axisymmetric code to generate downstream pressure input for computationally expensive Euler codes is discussed. A film supplement shows the calculation of the two operating points with the time-marching Euler code.

17. Key Words (Suggested by Author(s)) Computational fluid mechanics; Euler equations; Laser anemometry; Turbomachinery; Axial compressors		18. Distribution Statement Unclassified - unlimited STAR Category 02	
19. Security Classif. (of this report) Unclassified	20. Security Classif. (of this page) Unclassified	21. No. of Pages 20	22. Price* A02

* For sale by the National Technical Information Service, Springfield, Virginia 22161

NASA-Langley, 1982